



Enhancing Tunnel Stability Under High Ground Stress: Rheological Analysis and Support Strategies

Jiabing Zhang · Xu Xiang · Ronghuan Du  · Xiaohu Zhang

Received: 25 August 2023 / Accepted: 6 December 2023 / Published online: 10 February 2024
© The Author(s), under exclusive licence to Springer Nature Switzerland AG 2024

Abstract Aiming at the large deformation of surrounding rock during tunnel construction under high ground stresses, this paper takes a high ground stress soft rock tunnel project in Yunnan Province as the background. According to the uniaxial and triaxial compression and creep experiments of rock, a creep constitutive damage model suitable for this project is built. Then, this creep damage constitutive model is applied in FLAC3D numerical analysis software to analyze the deformation characteristics of each monitoring point of the tunnel and the plastic zone change characteristics of the surrounding rock during tunnel excavation during tunnel excavation, and a support optimization scheme is proposed for the project. The results show that the numerical calculation results are consistent with the actual monitoring data, which confirms the accuracy and rationality of the proposed creep constitutive model. In addition, when the tunnel is under different stress states, the location of the largest displacement deformation of the tunnel varies. Under self-weight stress, the maximum deformation

is located at the vault and invert, while under tectonic stress, the maximum deformation is located near the spandrel and haunch. Finally, according to the numerical calculation results under different working conditions, the optimized support schemes for the two working conditions are proposed respectively. Adopting combined group anchor surrounding rock reinforcement technology and constructing the inverted arch pipe pile, so that the shallow surrounding rock and deep surrounding rock together to form a complete system of coordinated deformation, and the use of large stiffness double-layer primary support technology to improve the ability of the primary support to absorb the deformation, which effectively reduces the creep characteristics of the surrounding rock, to control the large deformation of the tunnel. The research results of this paper can provide a reference for the support design of high geostress tunnels.

Keywords High geostress · Creep experiment · Support optimization · Double primary support · Numerical simulation

J. Zhang · X. Xiang · R. Du (✉) · X. Zhang
School of Civil Engineering and Architecture, Guangxi University, Nanning 530004, China
e-mail: ronghuan.du.work@outlook.com

J. Zhang
e-mail: zhang.j.b@gxu.edu.cn

J. Zhang
Key Laboratory of Disaster Prevention and Structural Safety, Guangxi University, Nanning 530004, China

1 Introduction

The large deformation of tunnels under high ground stresses has always been a major problem in tunnel engineering (Chen et al. 2022). However, there are many mountainous areas in Northwest and Southwest China, and the geological conditions are relatively

complex. With the in-depth promotion of national western development, the Belt and Road Initiative and other major strategies, many tunnel projects have emerged in western mountainous areas (Zhang et al. 2022a; Li et al. 2020a, b). These mountain tunnel projects generally encounter weak strata such as weak interlayer zones, which are buried deep and bear complex geological tectonic movements (Sun et al. 2018). If not handled properly, then these projects are prone to undergo damage to the supporting structure, large deformation collapse and other disasters (Li et al. 2020a, b).

Aiming at the problem of the large deformation of soft rock tunnels under high ground stresses, Chinese scholars have conducted in-depth research on the deformation characteristics and optimization support schemes of typical large-deformation tunnels (Bao et al. 2022; Chen et al. 2019; Deng et al. 2022; He et al. 2022; Liu et al. 2022a, b; Meng et al. 2013; Wang et al. 2021a, b; Zhang et al. 2022a, b, c, d; Zhang et al. 2022b). The above tunnels are mostly located in mountains and at large burial depths, and the surrounding rock lithology of the tunnels is mainly soft rock. Under the action of high ground stress, the tunnels have undergone great deformation (Chen et al. 2021; Zhang et al. 2021). To better understand the actual deformation characteristics of such tunnels, scholars have mainly examined the factors affecting deformation through experiments or numerical simulations based on the analysis of on-site deformation monitoring data, combined with the characteristics of actual tunnel engineering lithology, stress, etc., and have proposed and analyzed the effect of countermeasures to reduce tunnel deformation (Tian et al. 2022; Xu, et al. 2022; Yang et al. 2018). The above studies have enriched our understanding of large tunnel deformation under high ground stresses and have contributed to further research on tunnel deformation.

In addition, the measured data of large tunnel deformation are often related to the rheological characteristics of the surrounding rock; that is, the deformation of a data monitoring point is often not static but has a certain time effect (Gutierrez-Ch et al. 2022; Xu and Gutierrez 2021). However, it is difficult for scholars to form a unified theory to quantitatively describe the rheological characteristics of all of the surrounding rock of the tunnel. Therefore, most researchers

have investigated the creep characteristics and constitutive equations of rock samples collected in the field to explore the rheological characteristics of tunnel surrounding rock (Ji et al. 2020; Jia et al. 2018; Liu et al. 2020; Wang et al. 2021a, b). For instance, in terms of the creep characteristics of rocks, most of the current research focuses on the creep characteristics of the same type of rocks under different working conditions or the creep characteristics of different types of rocks (Niu et al. 2021; Sabitova et al. 2021; Qiao et al. 2022). In terms of rock creep constitutive model, scholars mainly use the combination of mechanical components to form the creep constitutive model, and introduce the damage factor to establish the creep damage constitutive model that can reflect the various creep stages of the rock (Okuka et al. 2019; Frenelus et al. 2022; Kamdem et al. 2023). To date, research studies of creep models have mainly focused on the mechanical properties and parameter analyses of the creep behavior of a single rock (Hou et al. 2019; Taheri et al. 2020). However, there is a lack of practical engineering case studies for this model, such as extending the creep model of rock to the mechanical response during actual tunnel excavation and operation (Oggeri et al. 2022; Xu et al. 2020; Yin et al. 2022). And the research on the optimization of tunnel support measures mostly focuses on the single stress situation, and lacks the research in complex situations, such as the reasonable optimization of support measures in complex geological situations (Sun et al. 2023; Yu et al. 2020; Azad et al. 2023).

Therefore, to explore the rheological characteristics of tunnels under high ground stresses, in this study, uniaxial and triaxial compression creep tests of natural rock samples were carried out based on the actual project of a tunnel in Yunnan Province, China. On this basis, a fractional-order creep damage model reflecting the characteristics of different creep stages of different natural rocks was obtained by connecting classical mechanical components based on fractional-order theory and strain control. In addition, parameter identification was conducted according to the experimental data to verify the rationality of the model. Finally, via finite difference software, the proposed constitutive model was used to analyze the long-term stability of different tunnels under the action of high ground stress, and

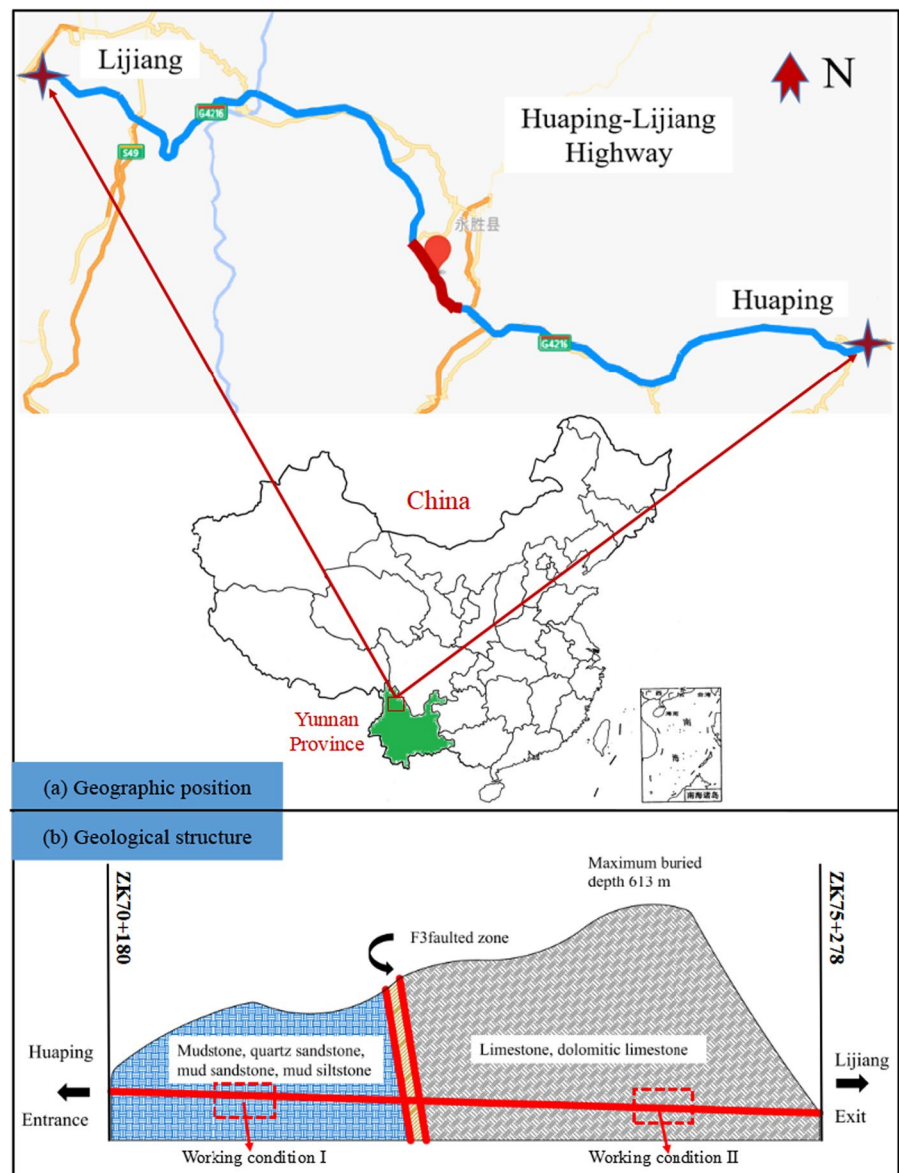
corresponding support optimization measures were proposed according to the tunnel deformation under different ground stresses. The conclusions of this paper can provide theoretical support for the design and construction of tunnels under high ground stresses.

2 Project Overview

2.1 Engineering Background

As shown in Fig. 1, the tunnel is located in Lijiang city, Yunnan Province, and is an important part of the Huaping-Lijiang Expressway. The starting and ending points of the left line of the bid section are ZK70+180~ZK75+278, and the total length of the demarcation section is 5098 m. The starting and ending pile numbers of the right line are YK70+130~YK75+335, and the total length of the

Fig. 1 Geographic position and geological structure of the tunnel



boundary section is 5205 m. The altitude is between 1869.951 and 2512.482 m, and the relative height difference is approximately 642.53 m. The geological conditions of the tunnel are complex, with engineering problems such as faults, karsts, and landslides. The surrounding rock of the tunnel is mainly (approximately 70%) grade IV and grade V. The maximum burial depth of the tunnel is approximately 613 m, and it passes through the F3 fault section, which is an active Holocene seismogenic fault. The width of the fault zone is approximately 95 m, and the fault occurrence is $310^\circ \angle 72^\circ$, indicating a compressive reverse fault. According to the geological exploration data, taking the F3 fault section as the boundary, the lithology of the surrounding rock at the entrance of the Huaping direction of the tunnel is mainly mudstone, mixed with quartz sandstone, argillaceous sandstone and argillaceous siltstone. The lithology of the surrounding rock at the outlet of the Lijiang direction is mainly limestone and dolomitic limestone, as shown in Fig. 1b. The lithologies of the surrounding rock on the two sides of the fault are quite different, but these rocks are mainly metamorphic rocks represented by mudstone and limestone, with the characteristics of rock mass fragmentation and obvious rheological properties.

2.2 Construction Techniques

The construction technology of the tunnel is mainly based on the three-bench excavation method, and the excavation process is as follows:

- 1.1.1. First, the upper bench is excavated, and the initial support of the upper hole structure is applied after the completion of the upper excavation. That is, 4 cm thick concrete is initially sprayed, and the steel frame is erected. Then, the system anchor is drilled and resprayed to the design thickness, and the bench height is approximately 3.4 m.
- 2.2.2. After the construction of the upper bench to 3~5 m, the middle bench is excavated, the steel frame is extended, and the initial support and bottom sealing of the tunnel structure are applied. The process is the same as that of the upper bench, and the height of the bench is approximately 3.0 m.

3.3.3. After 5~8 m of excavation of the middle bench, the lower bench is excavated, and the initial support is closed in time. The process is the same as that of the upper bench, and the height of the bench is approximately 3.0 m. After the excavation of the lower bench is completed, the inverted arch and the tunnel bottom are filled in time;

4.4.4. Finally, the lining template trolley is used to construct the secondary lining (the arched wall lining is constructed once).

The support measures of the tunnel adopt the anchor spray support method, and the support parameters are shown in Table 1.

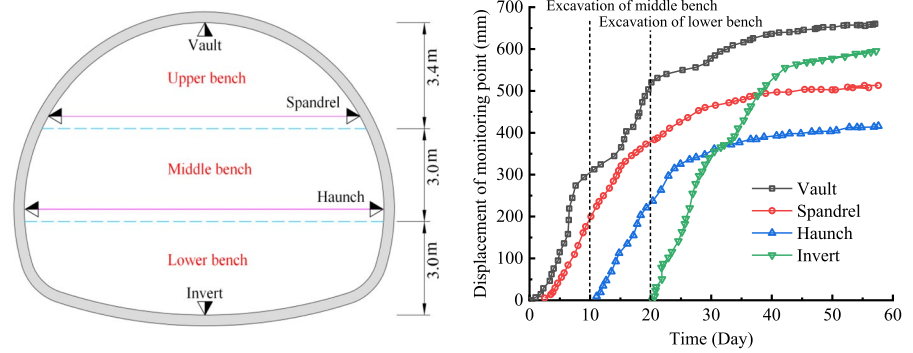
2.3 Deformation Characteristics and Stress Environment

The surrounding rock of the tunnel is mainly composed of level five surrounding rock and level four surrounding rock, which exhibit rheological, volume, hydrological changes and have poor self-stability characteristics. After applying certain support measures to the tunnel after excavation, disasters such as cracking of the initial support shotcrete, block falling, arch shoulder cracking, deformation of the arch waist, and uplift and deformation of the arch bottom occurred in some locations over time. Figure 2 shows the time history curve of a section of the tunnel. Within 60 days after the three-bench excavation, the final value of vault settlement is 660.46 mm, the final value of spandrel settlement is 512.99 mm, the horizontal convergence value of the haunch is 416.08 mm, and the uplift value of the inverted arch at the arch bottom is 595.15 mm. This shows that

Table 1 Supporting structure design parameters

Supporting structure	Design parameter
Advanced small pipe	A42, L=450 cm, 180 cm×30 cm
Primary support	Shotcrete: C25; Thickness=27 cm Steel mesh: A8@15 cm×15 cm Steel rib: I20a@60 cm Hollow grouted bolt: A25, L=450 cm, and 100 cm×50 cm Deformation allowance: 15 cm
Secondary lining	Concrete: C35; Thickness=70 cm Deformation allowance: 50 cm

Fig. 2 On-site monitoring points and section deformation monitoring results of the tunnel



after the completion of excavation, the deformation of the surrounding rock is large with characteristics of rheological changes, which seriously endangers the safety of construction personnel.

The tunnel is bounded by the F3 fault zone, and the lithologic characteristics on both sides of the fault are quite different. The in situ stress of the surrounding rock at the entrance of the tunnel in the Huaping direction is mainly self-weight stress. The field monitoring data show that the measured in situ stress of the vault is approximately 7 MPa, the measured in situ stress near the horizontal arch waist is approximately 2 MPa, and the lateral pressure coefficient is approximately 0.3. The in situ stress of the surrounding rock at the exit end of the tunnel in the Lijiang direction is mainly horizontal tectonic stress, with a horizontal tectonic stress of approximately 17.52 MPa and a vertical tectonic stress of approximately 14.79 MPa. Therefore, the in situ stress environment of the tunnel is relatively

harsh, and the deformation and failure modes may change with increasing tunnel depth.

Based on the engineering background, taking the F3 fault zone as the boundary, two calculation conditions of the self-weight stress field and tectonic stress field are constructed, which are divided into working condition I and working condition II, respectively. Figure 3 shows the ground stress on the two working conditions, where σ_x and σ_z are the horizontal and vertical components of the ground stress, respectively.

3 Creep Test and Constitutive Equation

3.1 Experimental Scheme

It can be seen from the second section of this paper that the surrounding rock of the tunnel is mainly mudstone and dolomite limestone, so the rock samples used in the creep test are taken from the tunnel site.

Fig. 3 Illustration of the geostress field

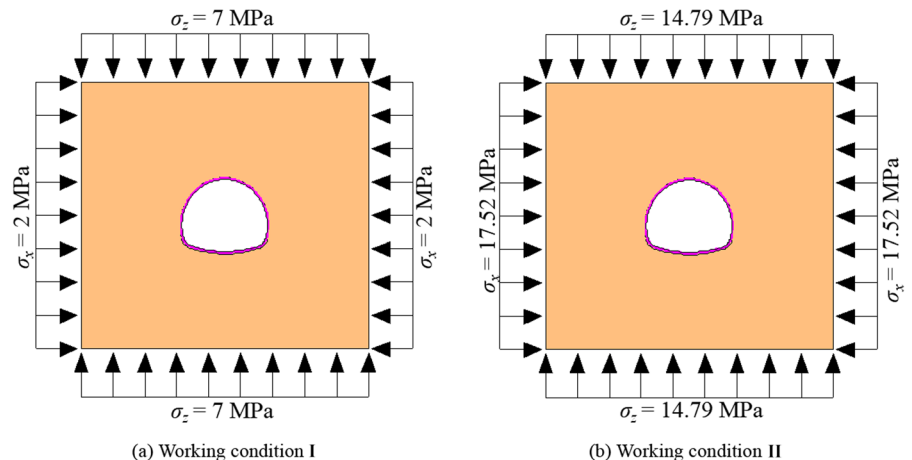




Fig. 4 Test equipment and specimen loading

Table 2 Strength of rock specimens under different confining pressures

Rock sample	Confining press (MPa)	Strength (MPa)	Rock sample	Confining press (MPa)	Strength (MPa)
Mudstone	0	18.54	Limestone	0	66.88
	2	23.59		8	94.19
	4	29.38		15	115.24

Through the drilling core sampling, indoor cutting, grinding and other processes, the rock is processed into a standard sample with a diameter of 50 mm and a height of 100 mm. Figure 4 shows the experimental equipment and experimental loading diagram. Before the creep test, it is necessary to determine the grading

load loading grade of a rock sample. Therefore, three mudstones and three limestones are selected for uniaxial and triaxial compression tests to determine the compressive strength of the rock. The strength values of the mudstones and limestones under different confining pressures are shown in Table 2.

For the creep test, three mudstone and three limestone samples are selected, and the compression creep test of the rock samples under the same confining pressure is set according to the uniaxial and triaxial compressive strength obtained by conventional compression testing. The loading level of the preset rock sample is 0.15, 0.30, 0.45, 0.60, 0.75, and 0.90 times the strength under the corresponding confining pressure conditions, which is divided into 6 levels of loading, as shown in Table 3.

Table 3 Rock creep loading stress grade under different confining pressures

Rock sample	Confining pressure (MPa)	Stress levels at all levels of loading (MPa)					
		1	2	3	4	5	6
Mudstone	0	2.78	5.56	8.34	11.12	13.90	16.69
	2	3.54	7.08	10.62	14.15	17.69	21.23
	4	4.41	8.81	13.22	17.63	22.03	26.44
Limestone	0	10.03	20.06	30.09	40.13	50.16	60.19
	8	14.13	28.26	42.39	56.51	70.64	84.77
	15	17.29	34.57	51.86	69.14	86.43	103.72

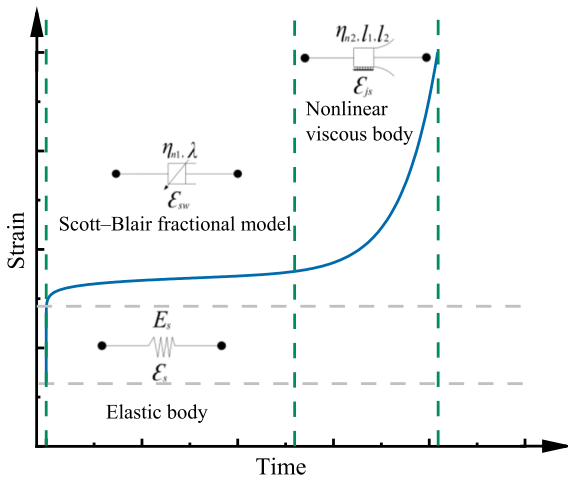


Fig. 5 Creep theory process curve

3.2 Creep Damage Constitutive Equation

The results of the triaxial compression creep tests of the rock samples show that the creep loading curve of rock samples is composed of instantaneous elastic deformation, attenuation creep deformation, stable creep deformation and accelerated creep deformation, and the constitutive relationship of instantaneous creep deformation ϵ_s can be expressed by the elastomer constitutive relationship. The constitutive relationship of the sum ϵ_{sw} of the attenuation creep deformation and the stable creep deformation can be expressed by the Scott-Blair model (Wu et al. 2020). When the strain of the rock sample reaches a certain threshold, the creep deformation of the rock sample rapidly enters the stage of accelerated creep from stable creep deformation, so the constitutive relationship of creep deformation ϵ_{js} at this stage can be represented by a nonlinear creep body with strain triggering, as shown in Fig. 5.

The constitutive equation of instantaneous elastic deformation ϵ_s can be expressed as

$$\epsilon_s = \frac{\sigma_0}{E_s} \tag{1}$$

where σ_0 is the long-term load and E_s is the elastic modulus of the elastomer.

The constitutive equation of the sum of decay creep deformation and steady creep deformation ϵ_{sw} is represented by the Scott-Blair model (Wang and Zhou 2020; Gao and Yin 2021), The creep equation expression of the Scott-Blair fractional element can be obtained by integrating the fractional calculus with the Riemann–Liouville fractional operator(Liu et al. 2022a, b; Zhang et al. 2022a, b, c, d)

$$\epsilon_{sw} = \frac{\sigma_0}{\eta_{n1}} \frac{t^\lambda}{\Gamma(1 + \lambda)} \tag{2}$$

where, $\Gamma(\lambda) = \int_0^\infty t^{\lambda-1} e^{-t} dt$ ($t > 0$), η_{n1} is the viscosity coefficient of the material, λ is the fractional order, and $0 \leq \lambda \leq 1$.

In this paper, the strain parameter is used to characterize whether the rock enters the accelerated creep stage. An improved nonlinear creep body with strain triggering is introduced to describe the deformation of the rock in the accelerated creep stage (Jiang et al. 2013). Let η_{n2} be the nonlinear viscosity coefficient and l_1 be the creep parameter. The constitutive relation of the nonlinear viscous cylinder is defined as

$$\begin{cases} \epsilon = \exp\left(\frac{\sigma_0}{\eta_{n2} l_1} t + \ln l_2\right) & (\epsilon \geq \epsilon_a) \\ \epsilon = 0 & (\epsilon < \epsilon_a) \end{cases} \tag{3}$$

In the formula, η_{n2} is a nonlinear viscosity coefficient, l_1 and l_2 are creep parameters, and ϵ_a is the strain threshold.

Therefore, according to the viewpoint of rock rheological mechanics, the time-dependent deformation characteristics of rock under long-term loading can be quantitatively described by connecting the abovementioned spring body, Scott-Blair fractional order element and strain-triggered improved nonlinear creep body in series to form a strain-controlled constitutive model that can characterize the creep deformation of rock under the time effect. Therefore, the one-dimensional creep total strain expression of the rock sample is

$$\begin{cases} \epsilon(t) = \frac{\sigma_0}{E_s} + \frac{\sigma_0}{\eta_{n1}} \frac{t^\lambda}{\Gamma(1+\lambda)} & (\epsilon < \epsilon_a) \\ \epsilon(t) = \frac{\sigma_0}{E_s} + \frac{\sigma_0}{\eta_{n1}} \frac{t^\lambda}{\Gamma(1+\lambda)} + \exp\left(\frac{\sigma_0}{\eta_{n2} l_1} t + \ln l_2\right) & (\epsilon \geq \epsilon_a) \end{cases} \quad (4)$$

In addition to the uniaxial compression creep test, the triaxial compression creep test is also carried out in this study, so it is necessary to expand Eq. (4) in three dimensions. According to the theory of elastic mechanics, the stress tensor σ_{ij} can be decomposed into the stress spherical tensor σ_m and the partial tensor S_{ij} , and the strain tensor ϵ_{ij} can be decomposed into the strain spherical tensor ϵ_m and the partial tensor e_{ij} .

$$\begin{cases} \sigma_{ij} = \delta_{ij} \sigma_m + S_{ij} \\ \epsilon_{ij} = \delta_{ij} \epsilon_m + e_{ij} \end{cases} \quad (5)$$

where δ_{ij} is the Kronecker delta.

According to the generalized Hooke’s law, the three-dimensional constitutive relation of an elastic body is

$$\epsilon_{ij}^s = \frac{S_{ij}}{2G_s} + \frac{\sigma_m \delta_{ij}}{3K_s} \quad (6)$$

where ϵ_{ij}^s is the strain of the elastomer, and G_s and K_s are the elastic shear modulus and bulk modulus, respectively.

For Scott-Blair model elements, the three-dimensional constitutive relation is

$$\epsilon_{ij}^{sw}(t) = \frac{S_{ij}}{2G_{sw}} \frac{t^\lambda}{\Gamma(1+\lambda)} \quad (7)$$

where $\epsilon_{ij}^{sw}(t)$ is the strain of the fractional element, and G_{sw} is the viscous shear modulus.

For a strain-triggered improved nonlinear creep body, its three-dimensional constitutive relation is

$$\epsilon_{ij}^{js} = \begin{cases} \exp\left(\frac{S_{ij}}{2\eta_{n2} l_1} t + \ln l_2\right) & (\epsilon \geq \epsilon_a) \\ 0 & (\epsilon < \epsilon_a) \end{cases} \quad (8)$$

Therefore, the triaxial loading creep constitutive equation of the rock sample is

$$\epsilon_{ij}(t) = \begin{cases} \frac{S_{ij}}{2G_s} + \frac{\sigma_m \delta_{ij}}{3K_s} + \frac{S_{ij}}{2G_{sw}} \frac{t^\lambda}{\Gamma(1+\lambda)} & (\epsilon < \epsilon_a) \\ \frac{S_{ij}}{2G_s} + \frac{\sigma_m \delta_{ij}}{3K_s} + \frac{S_{ij}}{2G_{sw}} \frac{t^\lambda}{\Gamma(1+\lambda)} + \exp\left(\frac{S_{ij}}{2\eta_{n2} l_1} t + \ln l_2\right) & (\epsilon \geq \epsilon_a) \end{cases} \quad (9)$$

Under the condition of a constant confining pressure creep test, $\sigma_2 = \sigma_3$,

$$\begin{cases} \sigma_m = \frac{1}{3}(\sigma_1 + \sigma_2) \\ S_{11} = \sigma_1 - \sigma_m = \frac{2}{3}(\sigma_1 - \sigma_3) \\ S_{22} = \sigma_2 - \sigma_m = \frac{1}{3}(\sigma_3 - \sigma_1) \end{cases} \quad (10)$$

Therefore, the axial creep equation based on Eqs. (9) and (10) is

$$\epsilon_{ij}(t) = \begin{cases} \frac{\sigma_1 - \sigma_3}{3G_s} + \frac{\sigma_1 + 2\sigma_3}{9K_s} + \frac{\sigma_1 - \sigma_3}{3G_{sw}} \frac{t^\lambda}{\Gamma(1+\lambda)} & (\epsilon < \epsilon_a) \\ \frac{\sigma_1 - \sigma_3}{3G_s} + \frac{\sigma_1 + 2\sigma_3}{9K_s} + \frac{\sigma_1 - \sigma_3}{3G_{sw}} \frac{t^\lambda}{\Gamma(1+\lambda)} + \exp\left(\frac{\sigma_1 - \sigma_3}{3\eta_{n2} l_1} t + \ln l_2\right) & (\epsilon \geq \epsilon_a) \end{cases} \quad (11)$$

3.3 Parameter Identification and Model Validation

Due to space limitations, this paper only shows the creep model fitting parameters of mudstone and limestone under triaxial loading. Tables 4 and 5 show the creep model fitting parameters of mudstone and limestone under different confining pressures in the first five loading stages and the last loading stage, respectively, where L represents the loading grade, the specific stress applied to the rock samples under various working conditions under the loading grade is shown in the Table 3, and σ_3 represents the confining pressure. The bulk modulus G_s , elastic shear modulus K_s and viscous shear modulus G_{sw} of mudstone and limestone gradually decrease with increasing loading grade and confining pressure. The fractional order λ , viscosity coefficient η_{n2} , and creep parameters l_1 and l_2 have no obvious change trend with increasing loading level and confining pressure, which is related to the creep properties of rock samples. The strain threshold ϵ_a

Table 4 Creep model identification parameters for the first five loading levels

Rock type	<i>L</i>	Test specimen $\sigma_3 = 2$ MPa				Test specimen $\sigma_3 = 4$ MPa			
		G_s (GPa)	K_s (GPa)	G_{sw} (GPa·h)	λ	G_s (GPa)	K_s (GPa)	G_{sw} (GPa·h)	λ
Mudstone	1	4.53	2.73	9.93	0.05	3.83	2.05	9.15	0.09
	2	3.95	2.46	8.73	0.08	3.75	1.95	8.03	0.10
	3	2.85	1.76	7.69	0.11	3.05	1.52	7.35	0.11
	4	2.01	1.18	6.89	0.10	2.18	1.23	6.84	0.17
	5	1.52	0.97	6.04	0.13	1.57	1.01	5.74	0.13
Rock type	<i>L</i>	Test specimen $\sigma_3 = 8$ MPa				Test specimen $\sigma_3 = 15$ MPa			
		G_s (GPa)	K_s (GPa)	G_{sw} (GPa·h)	λ	G_s (GPa)	K_s (GPa)	G_{sw} (GPa·h)	λ
Limestone	1	10.03	5.83	15.06	0.08	9.03	5.73	15.11	0.07
	2	9.53	5.34	12.13	0.12	8.81	5.82	18.02	0.06
	3	8.06	4.29	11.63	0.11	6.71	4.69	13.15	0.12
	4	6.30	2.79	10.24	0.20	5.27	2.81	12.01	0.13
	5	4.76	2.09	9.54	0.22	5.07	2.21	10.55	0.15

Table 5 Creep model identification parameters for the last loading level

Rock type	σ_3 (MPa)	ϵ_a (10^{-2})	G_s (GPa)	K_s (GPa)	G_{sw} (GPa·h)	η_{n2} (GPa·h)	λ	l_1 (10^{-5})	l_2 (10^{-7})
Mudstone	2	1.05	1.28	0.73	4.98	94.8	0.14	7.21	0.82
	4	1.27	1.03	0.91	5.02	49.3	0.23	9.04	0.79
Limestone	8	1.63	3.86	1.49	9.03	75.3	0.21	9.72	0.32
	15	1.71	4.49	1.95	9.33	37.5	0.24	99.03	2.10

increases gradually with increasing confining pressure, which indicates that the creep deformation that can occur in rock samples increases with increasing confining pressure.

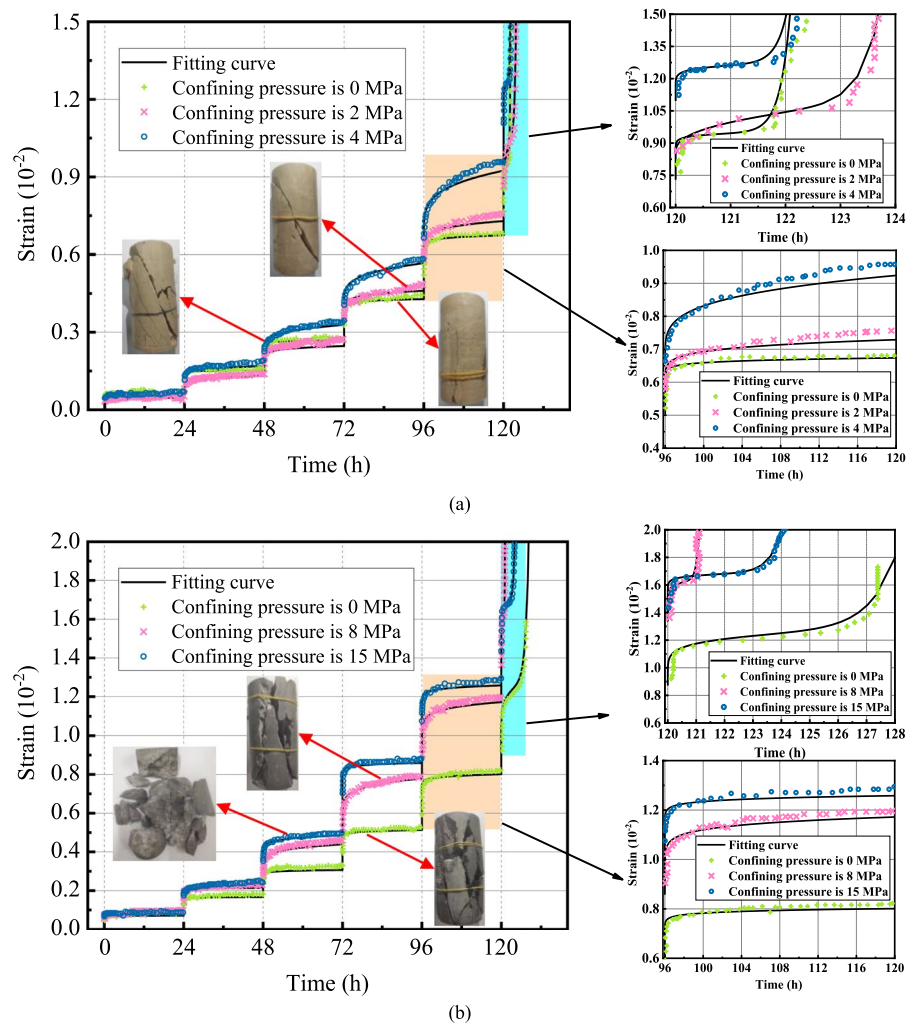
Figure 6 shows the comparison between the theoretical and experimental curves of creep of mudstone and limestone at different confining pressures. From the creep theoretical and experimental curves of mudstone under different confining pressures in Fig. 6a, it can be seen that the mudstone shows more obvious instantaneous elastic deformation of the specimen after each level of loading, which presents a larger creep increment on the creep curve. With the stress and time increase, the creep time curve shows decay creep and then enters the stable creep deformation stage. As the stress level continues to increase, the creep curve into the accelerated creep stage, and the specimen damage. Meanwhile, it can be seen that the creep deformation of the specimen increases with the increase of the

confining pressure. From Fig. 6b, it can be seen that the creep deformation curve trend of limestone is similar to that of mudstone. However, the difference is that the creep deformation of limestone increases more significantly with the increase of confining pressure during the creep test.

At the same time, from the specimen failure diagrams of mudstone and limestone in Fig. 6, it can be seen that the failure mode of mudstone and limestone during uniaxial creep test is characterized by failure with vertical cracks, while both samples show shear failure during triaxial creep test, and with the increase of the confining pressure the shear failure is more obvious, and the more friction traces on the shear surface.

The fitted parameters are substituted into Eqs. (4) and (11) to obtain the creep model curve. Then, based on the uniaxial and triaxial creep test data in this paper, the theoretical curve of the model is established with the test time as the independent variable and compared with the test data under

Fig. 6 Comparison of creep theoretical curves and experimental curves under different confining pressures for **a** mudstone and **b** limestone



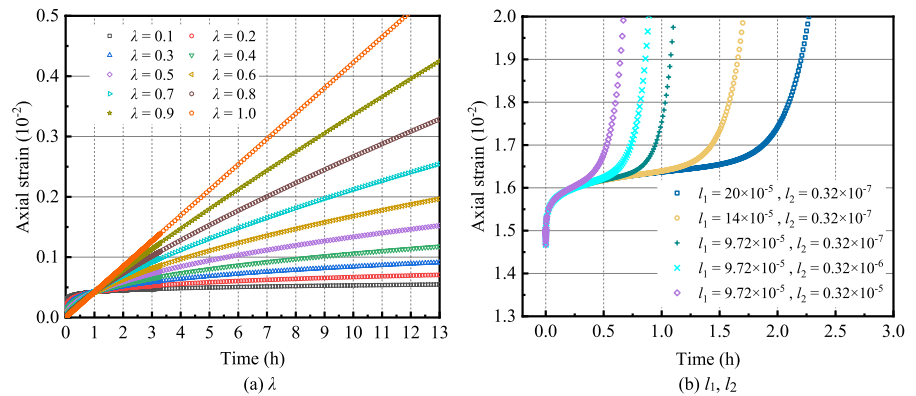
the same conditions, as shown in Fig. 6. From the comparison between the experimental data and the theoretical curve, it can be seen that the creep model under different confining pressures has a high degree of fitting with the creep test data of mudstone and limestone in the stable creep stage and the unstable creep stage and that the creep constitutive equation can better reflect the deformation and failure characteristics of mudstone and limestone from the first stage to the last stage of the loading process, which fully verifies the accuracy and applicability of the model.

3.4 Sensitivity Analysis of Parameters

The bulk modulus G_s , elastic shear modulus K_s , viscous shear modulus G_{sw} and viscosity coefficient η_{n2} in the constitutive equation are the parameters related to the physical and mechanical properties of the rock sample itself; these parameters characterize the ability of the rock sample to withstand load and deformation during creep. However, the fractional order λ and creep parameters l_1 and l_2 have no clear physical meaning, so it is necessary to carry out sensitivity analysis.

The parameters of limestone under the fifth load under a confining pressure of 8 MPa are substituted into the constitutive equation of the fractional-order element, and the creep curve cluster shown

Fig. 7 Sensitivity analysis of parameters



in Fig. 7a is obtained by giving different fractional orders λ . When λ is close to 0, the deformation of the material increases slowly for a period of time and then no longer changes, and the creep deformation in the stable stage approaches the horizontal line. When λ is close to 1, the material deforms continuously with the existence of a long-term load, and its creep curve is close to a straight line with a certain slope. Therefore, the fractional order λ determines the deformation scale of rock in the attenuation creep stage and steady creep stage.

The parameters of limestone under the last load step under a confining pressure of 8 MPa are substituted into the nonlinear creep body. By setting the same creep parameter l_1 to give different creep

parameters l_2 or setting the same creep parameter l_2 to give different creep parameters l_1 , the effects of l_1 and l_2 on the deformation of rock in the accelerated creep stage are discussed, as shown in Fig. 7b. When l_2 is the same, the time for the accelerated creep of rock becomes longer with increasing l_1 ; when l_1 is the same, the time for the accelerated creep of rock becomes shorter with increasing l_2 . Therefore, the creep parameters l_1 and l_2 determine the duration that the rock is in the accelerated creep stage. In summary, the creep constitutive equation proposed in this paper has fewer parameters and is easy to identify. The significance of each parameter is clear, which can truly reflect the creep characteristics of rock.

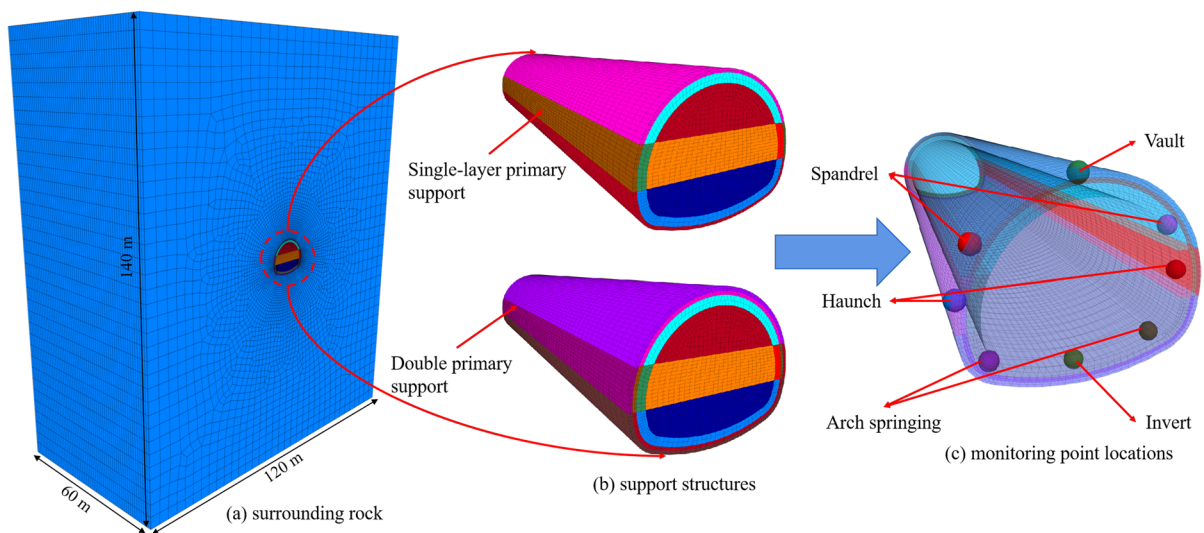


Fig. 8 Tunnel numerical model and monitoring points

4 Numerical Study of Different Support Schemes

4.1 Numerical Model and Parameters

In this research, a creep damage model was developed for the numerical simulation. According to engineering practice, the three-dimensional numerical calculation model of the tunnel is established by FLAC3D software. To eliminate the influence of the boundary on the calculation to a maximum extent, the model length \times width \times height is set as 120 m \times 60 m \times 140 m so that the model boundaries are 3–5 times the tunnel diameter in any dimension, as shown in Fig. 8. The bottom boundary of the model is fixed and constrained, the surrounding boundary constrains the normal displacement, and the self-weight of the overlying strata is replaced by the equivalent load. The model support measures reflect those used in engineering practice. The primary support and secondary lining are simulated by solid elements, and the leading small pipe and bolt are simulated by cable elements. The locations of the monitoring points were located at the vault, spandrel, haunch, arch springing and invert, respectively, as shown in Fig. 8c.

Based on the existing support scheme (Scheme I), a support optimization scheme (Scheme II and Scheme III) is proposed for tunnel construction under two different research working conditions. Among them, the advanced support uses a double-row advanced small pipe with a pipe length of 4.5 m. There are two layers of initial support. The first layer, with an initial support thickness of 31 cm, consists of C25 shotcrete. The second layer, with an initial support thickness of 27 cm, consists of C25 shotcrete. The second lining thickness is 70 cm, and consists of C35 shotcrete. A combination of long and short anchor bolts is adopted, both of which are applied after the initial support of the first layer is closed. To restrain the uplift of the tunnel arch bottom, inverted arch pipe piles are applied, and the lengths of the anchor bolts are all 10 m. The ground stress conditions and support schemes used in the numerical model are consistent with the schemes in Figs. 3 and 9, and the parameters of each support scheme are shown in Table 6. The model boundary conditions and tunnel excavation schemes for both working conditions in the numerical calculations are the same, and the construction is carried out according to Sect. 2.2 of this paper.

According to the field test results and indoor test data, the maximum principal stress in this area is between 7 and 17.52 MPa. Therefore, considering the most unfavorable situation, the second-stage load parameter with the enclosing pressure of 2 MPa is taken as the creep parameter under the condition of working condition I, and the first-stage load parameter with the enclosing pressure of 15 MPa is taken as the creep parameter under the condition of working condition II, as shown in Table 7.

4.2 Numerical Validation

As the macro-mechanical behavior of the rock mass depends on the microstructural parameters, the adopted parameters should be verified in the numerical simulation. So, the selected parameters are applied to the numerical model of the original support scheme (Scheme I) under the conditions of Working Condition I for calculation and verification. When the parameters in Table 7 are taken, the numerically calculated deformation distribution matches well with the field monitoring data, indicating that the secondary developed creep damage model is reliable and the numerical simulation calculation results are correct, as shown in Fig. 10.

5 Comparative Analysis of Numerical Results

5.1 Displacement Analysis of Tunnel Surrounding Rock

Figure 11 shows the numerical calculation results of the deformation distribution of the tunnel under the two working conditions of the original support scheme and the optimized support scheme. The numerical calculation results show that the maximum deformation of the tunnel is located at the vault and the invert under the self-weight stress condition, while it is located near the spandrel and the haunch under the tectonic stress condition. From Fig. 11, it can be seen that for the working condition I, after adopting the optimized support scheme, due to the imposition of inverted arch pipe pile, the anchor support in each part of the tunnel forms a complete system, and the effect of deformation coordination is strengthened, which effectively suppresses the uplift deformation of inverted arch and the tunnel deformation. Meanwhile,

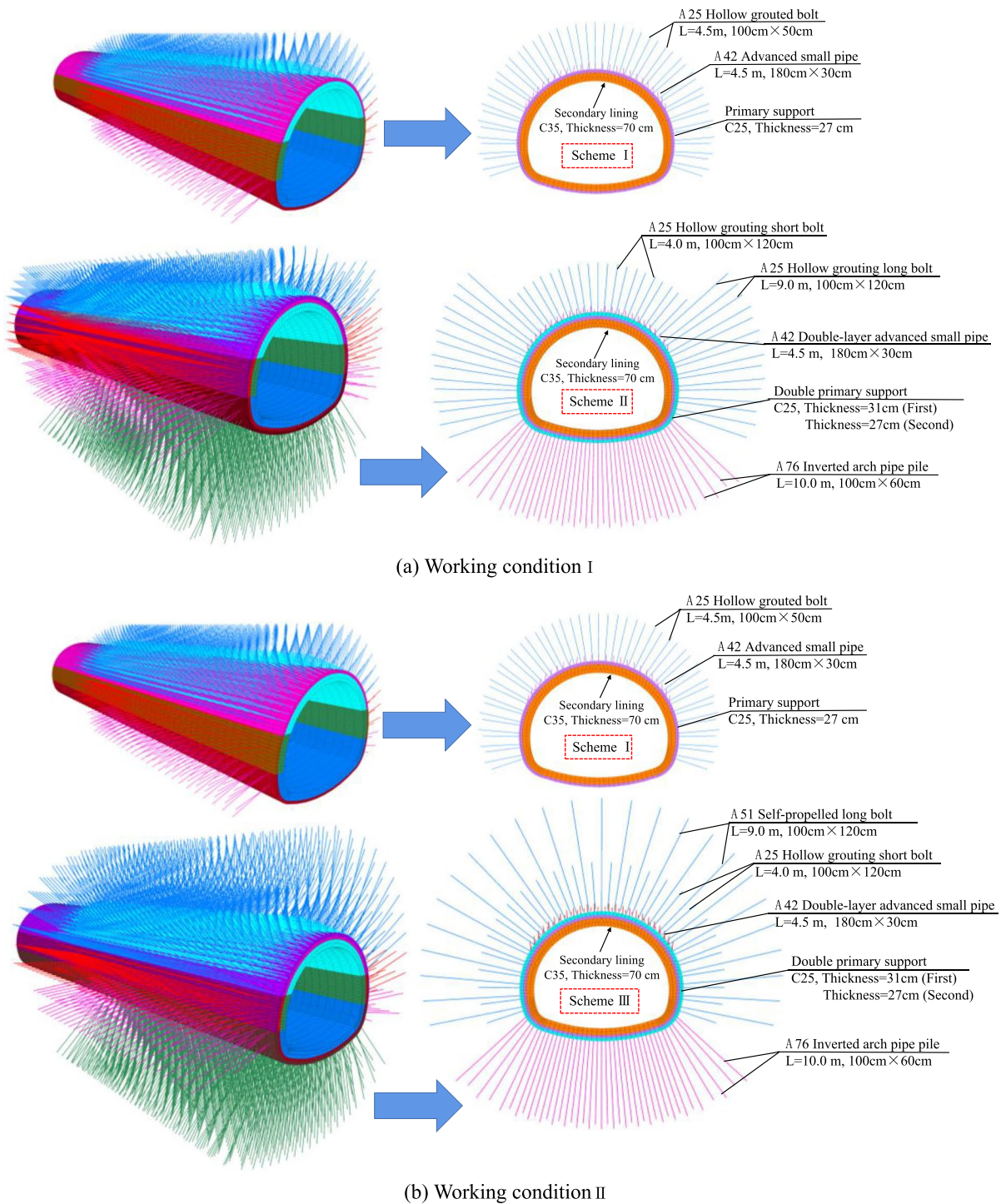


Fig. 9 Support schemes

Table 6 Material parameters of each support scheme

Type	Elastic modulus (GPa)	Bulk density (kN/m ⁻³)	Poisson's ratio
Advanced small pipe	210.0	–	0.30
C25 concrete	28.0	24.0	0.20
C35 concrete	31.5	25.0	0.20
Hollow grouted bolt	210.0	–	0.18
Self-propelled bolt	210.0	–	0.20
Inverted arch pipe	215.0	–	0.20

with the application of advanced pre-support and large stiffness double-layer initial support technology, the active control of plastic deformation of the surrounding rock and improve the ability of initial support to absorb deformation to further control the large deformation of the tunnel. For working condition II, as the tunnel is in the tectonic stress field, the horizontal principal stress is large at this time, and large deformation is likely to occur at the spandrel and haunch of the tunnel. Thus, on the basis of the

optimised support scheme in working condition I, the anchors at the vault and side wall adopt the combined group anchor reinforcement technology of combining long and short anchors, which is a reasonable combination of long and short anchors to form a group anchor effect, which can effectively limit the plastic deformation of the surrounding rock of the tunnel and inhibit the rate of deformation of the surrounding rock.

Table 8 shows the numerical calculation results of different monitoring points under each working condition. From Table 8, it can be seen that the convergence values of each monitoring point of the tunnel are effectively reduced after adopting the optimized scheme for each working condition, and the large deformation of the tunnel is effectively controlled. Under working condition I, the deformation values of the tunnel to the vault, shoulder, haunch and invert were reduced by 51.95%, 58.66%, 62.17% and 49.54% respectively compared with those without optimized support scheme at each monitoring point of the tunnel. For working condition II, after adopting the optimized support scheme, the deformation values of each monitoring point of the tunnel were reduced by 66.39%, 68.72%, 62.03% and 57.28%

Table 7 Creep parameters of surrounding rock in numerical simulation

Rock type	G_s (Gpa)	K_s (GPa)	G_{sw} (Gpa-h)	λ	ρ (Kg m ⁻³)	E (GPa)	μ	c (MPa)	φ (°)
Mudstone	3.95	2.46	8.73	0.08	2300	1.20	0.33	0.13	30
Limestone	9.03	5.73	15.11	0.07	2400	2.00	0.35	0.31	35

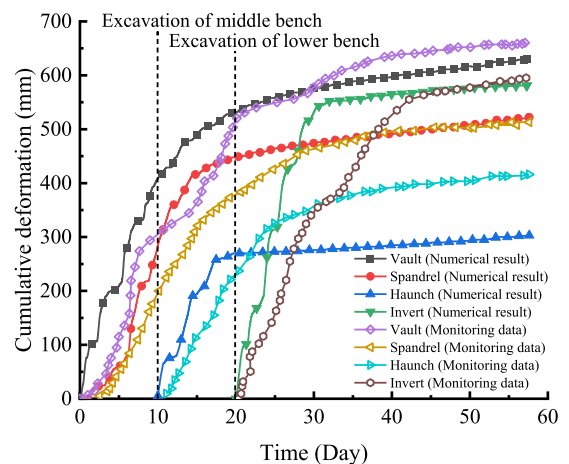
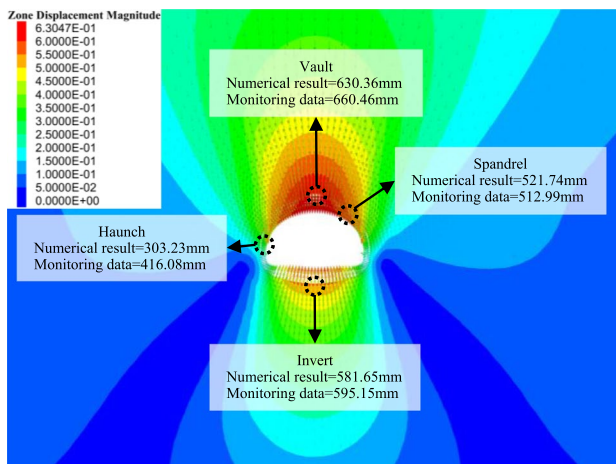
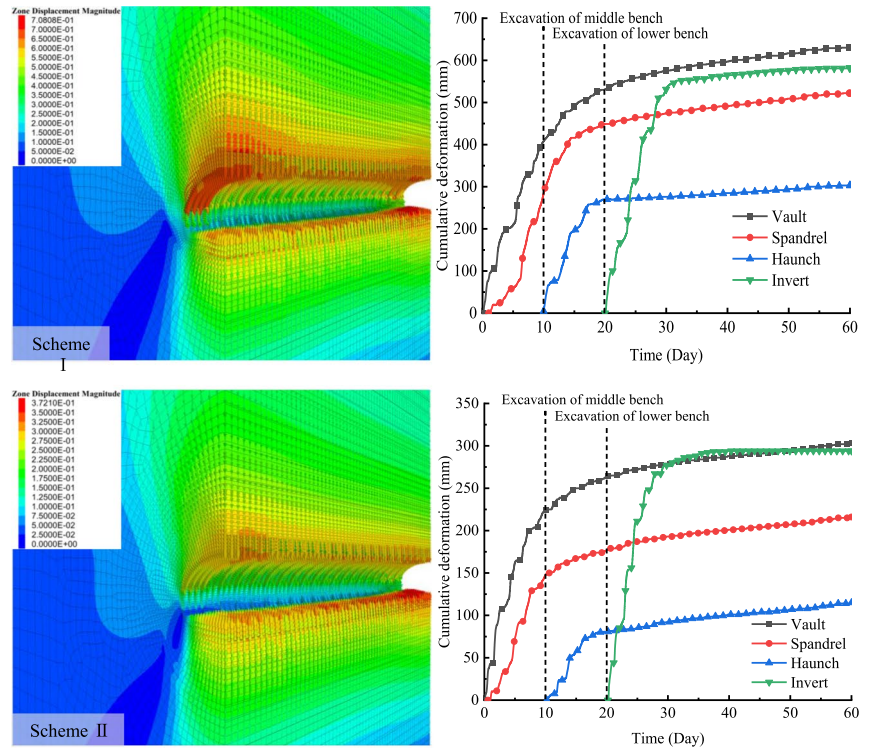
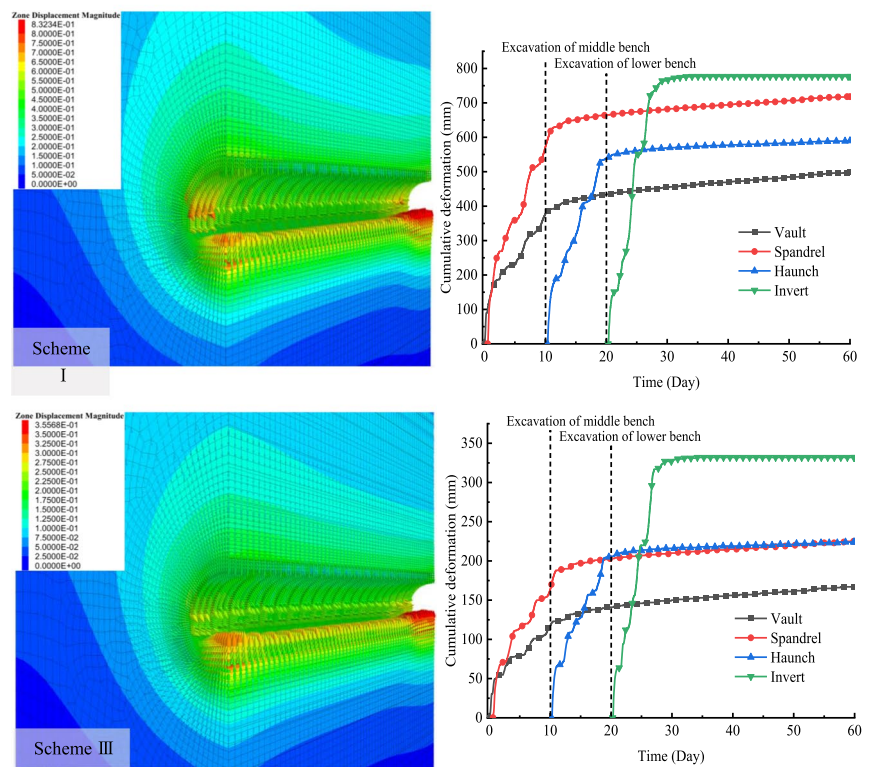


Fig. 10 Comparison between numerical simulation and field monitoring results

Fig. 11 Calculation results of deformation distributions using different support schemes



(a) Working condition I



(b) Working condition II

Table 8 Comparison of numerical results of monitoring points

Contrasting items	Working conditions	Monitoring points	Original scheme (mm)	Optimization scheme (mm)	Reduction rates (%)
Final displacement	Working condition I	Vault	630.36	302.90	51.95
		Spandrel	521.74	215.71	58.66
		Haunch	303.23	114.71	62.17
		Invert	581.65	293.52	49.54
	Working condition II	Vault	497.93	167.33	66.39
		Spandrel	718.30	224.67	68.72
		Haunch	589.98	224.04	62.03
		Invert	777.02	331.91	57.28

respectively. The optimized support scheme can be effectively applied to tunnel construction under two working conditions, which can significantly reduce the large deformation of the tunnel and control the convergence rate of the tunnel.

The optimization scheme can control the deformation of the tunnel, the main reasons are, increase the arrangement range of advance support, can more effectively improve the physical properties of the surrounding rock in front of the tunnel excavation, control the plastic deformation of the surrounding rock, reduce the disturbance of the surrounding rock in front of the excavation; Adopting combined group anchor rock reinforcement technology, combining long and short anchor rods with each other, and applying Inverted arch pipe pile to make the shallow and deep surrounding rocks work together to form a complete system of coordinated deformation; Finally, using large stiffness double-layer initial support technology, the initial support thickness increases, and its ability to absorb deformation is enhanced, thus maximizing the stability of the surrounding rock itself.

5.2 Analysis of Plastic Zone of Tunnel Surrounding Rock

Figure 12 shows the simulation results of the plastic zone for the two research working conditions. As shown in the figure, in the two working conditions of self-weight stress field and tectonic stress field, the surrounding rock after tunnel excavation mainly shows shear damage, from which the reason of inclined cracks in the lining is explained. From Fig. 12a, it can be seen that when the tunnel is in

the self-weight stress field, the plastic zone of the surrounding rock mainly appears around the tunnel vault and arch bottom. After adopting the optimized support scheme, the plastic zone of the surrounding rock around the vault and arch bottom of the tunnel is effectively reduced. As shown in Fig. 12b, the plastic zone around the tunnel is roughly circular in the tectonic stress field when the original support scheme is used. After using the optimized support scheme, the plastic zone appears irregularly round and the radius of the plastic zone is significantly reduced. At the same time, using the combination of long and short group anchor reinforcement measures, the extent of the plastic zone at the arch shoulder of the tunnel is significantly reduced. It can be seen that compared with the original support scheme, the optimized support scheme for each research condition can reduce the deformation and convergence of the tunnel and effectively control the large deformation of the tunnel.

In summary, the large deformation control measures of the tunnel are active reinforcement, stratified support, combined long and short, reduced disturbance, and reserved deformation.

6 Conclusion

The following conclusions can be drawn from the study of this paper.

- 1.1.1. Through a series of rock mechanics tests, according to the triaxial compression creep test results under different confining pressures, the rock shows obvious creep characteristics. The creep damage constitutive model was

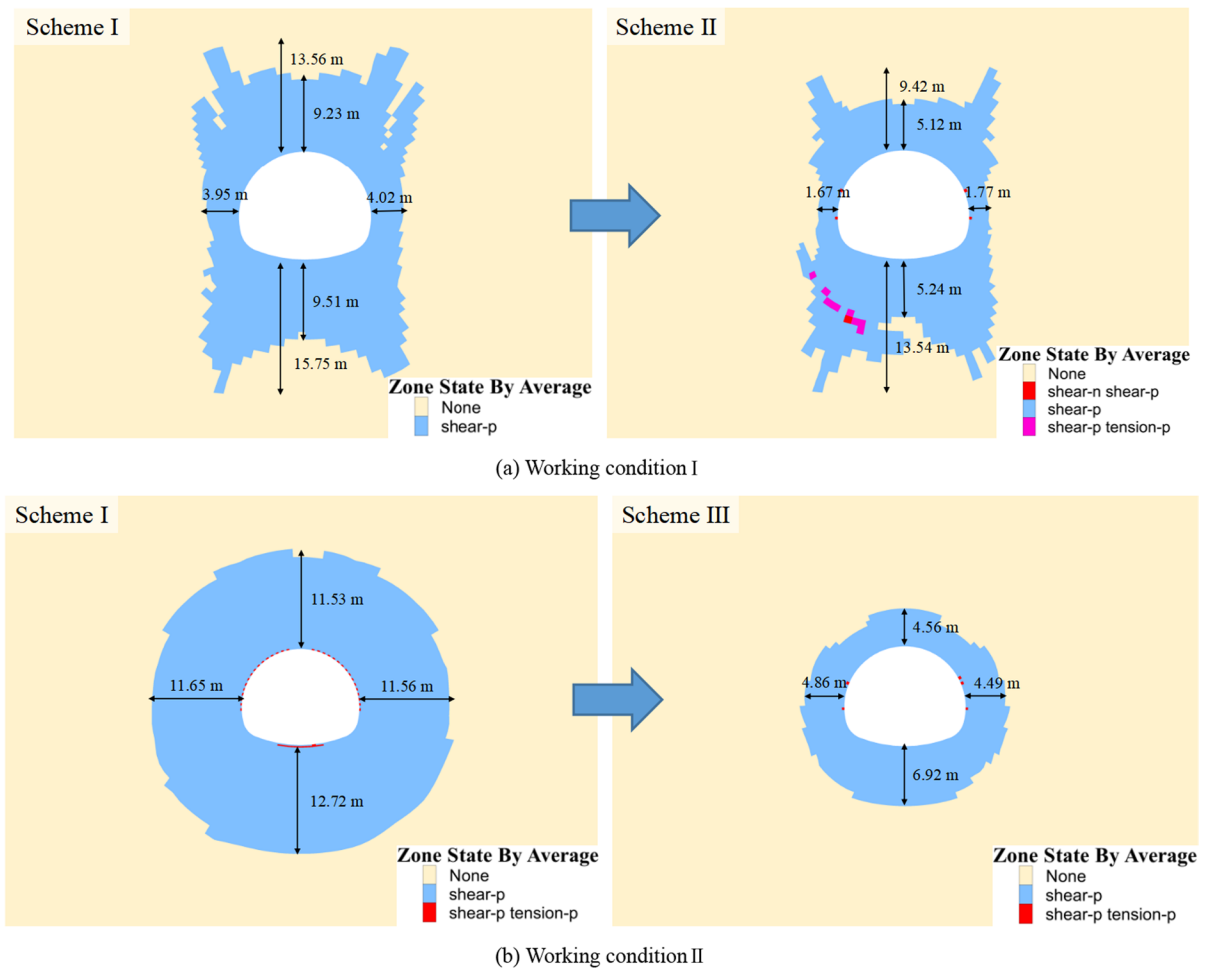


Fig. 12 Calculation results of plastic zones using different support schemes

established, and the surrounding rock parameters required for numerical calculation were determined by indoor creep experiments.

2.2.2. The creep damage constitutive model constructed in this paper can accurately reflect the creep characteristics of rock samples, and the derived constitutive equation has relatively few parameters that are easy to identify. The bulk modulus G_s , elastic shear modulus K_s and viscous shear modulus G_{sw} identified based on the test data gradually decrease with increasing loading level and confining pressure. The fractional order λ is the relevant parameter of the deformation scale of the rock in the attenuation creep stage and the steady-state creep stage, and the creep parameters l_1 and l_2 are the relevant

parameters of the duration that the of rock is in the accelerated creep stage.

3.3.3. The self-defined creep damage constitutive model was applied to the numerical calculation, and the numerical results were basically consistent with the actual monitoring data, which verified the reliability and rationality of the proposed creep damage constitutive model. The numerical calculation results show that the maximum deformation of the tunnel is located in the vault and shoulder under the self-weight stress and working conditions, while the maximum deformation of the tunnel is located in the shoulder and side wall under the tectonic stress working conditions. With the optimized support scheme, the deformation convergence

of the tunnel was effectively reduced under both working conditions.

- 4.4. Under working condition I, the tunnel vault settlement, side wall convergence and inverted arch uplift are reduced by 51.95%, 62.17% and 49.54%, respectively. Under working condition II, the tunnel vault settlement, side wall convergence and inverted arch uplift are reduced by 66.39%, 62.03% and 57.28%, respectively. And the plastic zone of the surrounding rock is significantly reduced after tunnel excavation, indicating that the tunnel construction process is safer and more controllable. Through using combined group anchor surrounding rock reinforcement technology, long and short anchors combined with each other, and applying inverted arch pipe piles, so that the shallow surrounding rock and deep surrounding rock together to form a complete system to coordinate the deformation, and the application of double-layer initial support, to improve the ability to absorb deformation, which can effectively control the large deformation of the tunnel.

Acknowledgements The authors express special thanks to the editors and anonymous reviewers for their constructive comments.

Authors Contribution Jiabing Zhang Methodology, Software, Writing. Xu Xiang Software, Writing. Ronghuan Du Validation, Investigation, Funding acquisition. Xiaohu Zhang Validation, Supervision.

Funding This study was financially supported by the National Natural Science Foundation of China (Grant No. 52108367), the Science and Technology Department of Guangxi Zhuang Autonomous (Grant No. AD21238018) and the Provincial Natural Science Foundation of Guangxi (Grant No. 2023GXNSFBA026260). The authors express special thanks to the editors and anonymous reviewers for their constructive comments.

Data availability Data will be available on request.

Declarations

Conflict of interest The authors declare that they have no known competing financial interests or personal relationships that could have appeared to influence the work reported in this paper.

References

- Azad MA, Naithani AK, Shekhar S et al (2023) Tunnel support validation using numerical modelling: a case study from NW, Himalaya, India. *Geotech Geol Eng* 41:4335–4349
- Bao H, Liu CQ, Liang N et al (2022) Analysis of large deformation of deep-buried brittle rock tunnel in strong tectonic active area based on macro and microcrack evolution. *Eng Fail Anal* 138:106351
- Chen ZQ, He C, Xu GW et al (2019) A case study on the asymmetric deformation characteristics and mechanical behavior of deep-buried tunnel in phyllite. *Rock Mech Rock Eng* 52:4527–4545
- Chen YX, Gao MZ, Li LP et al (2021) Contributory factors and distribution characteristics of asymmetric deformation in deep tunnel. *Geotech Geol Eng* 39:1223–1236
- Chen ZY, Wang ZX, Su GS et al (2022) Construction technology of micro bench cut method for weak rock tunnel with high in-situ stress. *Geotech Geol Eng* 40:1407–1415
- Deng HS, Fu HL, Shi Y et al (2022) Countermeasures against large deformation of deep-buried soft rock tunnels in areas with high geostress: a case study. *Tunn Undergr Sp Tech* 119:104238
- Frenelus W, Peng H, Zhang JY (2022) Creep behavior of rocks and its application to the long-term stability of deep rock tunnels. *Appl Sci-Basel* 12:17
- Gao YF, Yin DS (2021) A full-stage creep model for rocks based on the variable-order fractional calculus. *Appl Math Model* 95:435–446
- Gutierrez-Ch JG, Senent S, Zeng P et al (2022) DEM simulation of rock creep in tunnels using rate process theory. *Comput Geotech* 142:104559
- He MC, Sui QR, Li MN et al (2022) Compensation excavation method control for large deformation disaster of mountain soft rock tunnel. *Int J Min Sci Technol* 32:951–963
- Hou RB, Zhang K, Tao J et al (2019) A nonlinear creep damage coupled model for rock considering the effect of initial damage. *Rock Mech Rock Eng* 52:1275–1285
- Ji F, Li RJ, Feng WK et al (2020) Modeling and identification of the constitutive behavior of embedded non-persistent joints using triaxial creep experiments. *Int J Rock Mech Min* 133:104434
- Jia CJ, Xu WY, Wang RB et al (2018) Experimental investigation on shear creep properties of undisturbed rock discontinuity in Baihetan Hydropower Station. *Int J Rock Mech Min* 104:27–33
- Jiang QH, Qi YJ, Wang ZJ et al (2013) An extended Nishihara model for the description of three stages of sandstone creep. *Geophys J Int* 193:841–854
- Kamdem TC, Richard KG, Béda T (2023) New description of the mechanical creep response of rocks by fractional derivative theory. *Appl Math Model* 116:624–635
- Li ST, Tan ZS, Yang Y et al (2020a) Mechanical analyses and controlling measures for large deformations of inclined and laminar stratum during tunnelling. *Geotech Geol Eng* 38:3095–3112
- Li R, Han NN, Yuan CF et al (2020b) Analysis and design optimization of collapse characteristics of Taojiakuang tunnel entrance section. *Geotech Geol Eng* 38:551–560

- Liu JS, Jing HW, Meng B et al (2020) A four-element fractional creep model of weakly cemented soft rock. *B Eng Geol Environ* 79:5569–5584
- Liu WW, Chen JX, Luo YB et al (2022a) Long-term stress monitoring and in-service durability evaluation of a large-span tunnel in squeezing rock. *Tunn Undergr Space Technol* 127:104611
- Liu XL, Li DJ, Han C et al (2022b) A Caputo variable-order fractional damage creep model for sandstone considering effect of relaxation time. *Acta Geotech* 17:153–167
- Meng LB, Li TB, Jiang Y et al (2013) Characteristics and mechanisms of large deformation in the Zhegu mountain tunnel on the Sichuan-Tibet highway. *Tunn Undergr Space Technol* 37:157–164
- Niu SJ, Feng WL, Yu J et al (2021) Experimental study on the mechanical properties of short-term creep in post-peak rupture damaged sandstone. *Mech Time-Depend Mater* 25:61–83
- Oggeri C, Oreste P, Spagnoli G (2022) Creep behaviour of two-component grout and interaction with segmental lining in tunnelling. *Tunn Undergr Space Technol* 119:104216
- Okuka AS, Zorica D (2019) Fractional Burgers models in creep and stress relaxation tests. *Appl Math Model* 77:1894–1935
- Qiao LP, Wang ZC, Liu J et al (2022) Internal state variable creep constitutive model for the rock creep behavior. *B Eng Geol Environ* 81:11
- Sabitova A, Yarushina VM, Stanchits S et al (2021) Experimental compaction and dilation of porous rocks during Triaxial creep and stress relaxation. *Rock Mech Rock Eng* 54:5781–5805
- Sun XM, Chen F, Miao CY et al (2018) Physical modeling of deformation failure mechanism of surrounding rocks for the deep-buried tunnel in soft rock strata during the excavation. *Tunn Undergr Space Technol* 74:247–261
- Sun ZY, Zhang DL, Hou YJ et al (2023) Support countermeasures for large deformation in a deep tunnel in layered shale with high geostresses. *Rock Mech Rock Eng* 56:4463–4484
- Taheri SR, Pak A, Shad S et al (2020) Investigation of rock salt layer creep and its effects on casing collapse. *Int J Min Sci Technol* 30:357–365
- Tian XX, Song ZP, Wang HZ et al (2022) Evolution characteristics of the surrounding rock pressure and construction techniques: a case study from Taoshuping tunnel. *Tunn Undergr Space Technol* 125:104522
- Wang LY, Zhou FX (2020) Analysis of elastic-viscoplastic creep model based on variable-order differential operator. *Appl Math Model* 81:37–49
- Wang FN, Guo ZB, Qiao XB et al (2021a) Large deformation mechanism of thin-layered carbonaceous slate and energy coupling support technology of NPR anchor cable in Minxian Tunnel: a case study. *Tunn Undergr Space Technol* 117:104151
- Wang JB, Zhang Q, Song ZP et al (2021b) Experimental study on creep properties of salt rock under long-period cyclic loading. *Int J Fatigue* 143:106009
- Wu F, Gao RB, Liu J et al (2020) New fractional variable-order creep model with short memory. *Appl Math Model* 380:125278
- Xu GW, Gutierrez M (2021) Study on the damage evolution in secondary tunnel lining under the combined actions of corrosion degradation of preliminary support and creep deformation of surrounding rock. *Transp Geotech* 27:100501
- Xu GW, He C, Chen ZQ et al (2020) Transversely isotropic creep behavior of phyllite and its influence on the long-term safety of the secondary lining of tunnels. *Eng Geol* 278:105834
- Xu XY, Wu ZJ, Liu QS (2022) An improved numerical manifold method for investigating the mechanism of tunnel supports to prevent large squeezing deformation hazards in deep tunnel. *Comput Geotech* 151:104941
- Yang ZM, Wu SC, Gao YT et al (2018) Time and technique of rehabilitation for large deformation of tunnels in jointed rock masses based on FDM and DEM numerical modeling. *Tunn Undergr Space Technol* 81:669–681
- Yin ZC, Zhang X, Li XH et al (2022) Modified Burgers model of creep behavior of grouting-reinforced body and its long-term effect on tunnel operation. *Tunn Undergr Space Technol* 127:104537
- Yu KP, Ren FY, Puscasu R et al (2020) Optimization of combined support in soft-rock roadway. *Tunn Undergr Space Technol* 103:103502
- Zhang F, Liu JX, Zhang X et al (2021) Research on excavation and stability of deep high stress chamber group: a case study of Anju coal mine. *Geotech Geol Eng* 39:3611–3626
- Zhang B, Sun XM, Yang K et al (2022a) Model test study on large deformation mechanism of thin-bedded metamorphic sandstone tunnel. *B Eng Geol Environ* 81:436
- Zhang JB, Zhang XH, Huang Z et al (2022b) Transversely isotropic creep characteristics and damage mechanism of layered phyllite under uniaxial compression creep test and its application. *Environ Earth Sci* 81:499
- Zhang JB, Zhang XH, Chen W et al (2022c) A constitutive model of freeze–thaw damage to transversely isotropic rock masses and its preliminary application. *Comput Geotech* 152:105056
- Zhang L, Zhou HW, Wang XY et al (2022d) A triaxial creep model for deep coal considering temperature effect based on fractional derivative. *Acta Geotech* 17:1739–1751

Publisher's Note Springer Nature remains neutral with regard to jurisdictional claims in published maps and institutional affiliations.

Springer Nature or its licensor (e.g. a society or other partner) holds exclusive rights to this article under a publishing agreement with the author(s) or other rightsholder(s); author self-archiving of the accepted manuscript version of this article is solely governed by the terms of such publishing agreement and applicable law.

